Journal of Geophysical Research: Solid Earth

Supporting Information for

Impoundment-associated Hydro-mechanical Changes and Regional Seismicity near the Xiluodu Reservoir, Southwestern China

Man Zhang[1, 3], Shemin Ge[2], Qiang Yang[1], and Xiaodong Ma[3]

1 Tsinghua University, Department of Hydraulic Engineering, Beijing, China.

2 University of Colorado, Department of Geological Sciences, Boulder, United States.

3 ETH Zürich, Department of Earth Sciences, Zürich, Switzerland.

Contents of this file

Introduction

This supporting information shows the approach to solve the fault criticality in the Wudongde (WDD), Baihetan (BHT), and Xiluodu (XLD) area (Text S1); and the estimation of hydraulic diffusivity beneath the Xiluodu reservoir (Text S2).

This supporting information also provides the same figures (Figures S5 to S13) as seen in the main article, for Case A, C, D, and E; and the elastic stress changes induced by reservoir load for both thrust and right-lateral strike-slip faulting (Figures S14).

Text S1. Fault Criticality Analysis

The proximity of a fault (segment) to slip mainly depends on the stress field, fault geometry, Coefficient of friction (μ), and pore pressure (P_p). The Coulomb frictional failure criterion states that slip occurs if:

$$\tau_c = \mu \cdot \sigma_c \qquad (S1)$$

τ_c and σ_c are shear stress and (effective) normal stress along the critically stressed fault (Figure S1, red dot), respectively. For a given fault, its proximity to slip can be evaluated by the index of fault instability *I* proposed by Vavryčuk et al. (2013):

$$I = \frac{\tau - \mu(\sigma - \sigma_1)}{\tau_c - \mu(\sigma_c - \sigma_1)} \qquad (S2)$$

where τ and σ are the shear and (effective) normal traction along that fault (Figure S1, blue dot), respectively.

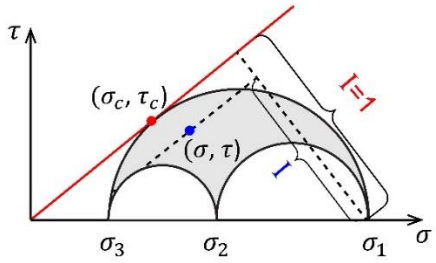

Figure S1. Definition of fault instability *I* in the context of Mohr diagram. The red dot marks the stress state on the optimally oriented fault, corresponding to fault instability *I* = 1. The blue dot marks the stress state on an arbitrarily oriented fault with fault instability *I* (modified from Vavrycuk (2014)).

We perform the iterative joint inversion for stresses using the MATLAB code 'STRESSINVERSE' developed by Vavrycuk (2014). Table S1 summarizes the inverted stress conditions in the Wudongde (WDD), Baihetan (BHT), and Xiluodu (XLD) areas, respectively. The stress inversion input via 'STRESSINVERSE' includes the strike, dip, and rake angles of both nodal planes of individual focal mechanism solutions. For each area, we use the available focal mechanism solutions of the M3+ earthquakes between 1936 and 2008 from the China Earthquake Networks Center (CENC), and the M2+ earthquakes between January 2016 and July 2019 (Duan, 2019). Table S1 shows the inverted orientations of effective principal stresses σ_1, σ_2, and σ_3, and stress shape ratio $R = (\sigma_2 - \sigma_1)/(\sigma_3 - \sigma_1)$ (Gephart & Forsyth, 1984).

Table S1. Results of stress inversions.

Study Area	Orientation of σ_1 (°)		Orientation of σ_2 (°)		Orientation of σ_3 (°)		R	Number of Focal Mechanisms
	Azimuth	Plunge	Azimuth	Plunge	Azimuth	Plunge		
XLD	113.2	4.9	21.7	16.4	219.3	72.8	0.81	117
BHT	130.8	3.4	33.7	64.4	222.4	25.4	0.77	367
WDD	143.8	6.6	45.7	50.6	239.1	38.6	0.71	42

To incorporate the uncertainty of parameters in Equation (S1), we follow Walsh and Zoback (Walsh & Zoback, 2016) to evaluate the fault criticality using the Monte Carlo method. The mean value of overburden stress (S_v) is estimated to be 135.7 MPa according to the average crustal density of 2.77 g/cm^3 (Zhu et al., 2017), and added Gaussian noise of standard deviation of 3 MPa and truncation of 10 MPa. We assign a uniform distribution of pore pressure (P_p) between 46.6 and 51.5 MPa, with the mean being hydrostatic at 5 km depth. The distribution of Coefficient of friction (μ) is taken from laboratory friction measurements on wet Westerly granite (Blanpied et al., 1995). We add Gaussian noise of standard deviation of 2° and truncation of 5° to the strike of all mapped fault segments. We assume the NNW- and NS-striking faults are W-dipping, and NE-striking faults are NW-dipping, as the majority of them do. We assign a uniform distribution of dip angle between 30° and 90°, corresponding to the range of typical dip angles of thrust fault and strike-slip fault. Table S2 summarizes the uncertainties associated with each parameter, which are consistently adopted for each area.

It is noted that the orientations of σ_1 are subhorizontal, while the inclination of stress axes of σ_2/σ_3 from the vertical can not be ignored. Thus, we first transform the stress tensor in principal directions to the geographical coordinate system (Zoback, 2007):

$$\boldsymbol{\sigma_g} = \boldsymbol{R} \cdot \boldsymbol{\sigma} \cdot \mathbf{R}^{\boldsymbol{T}} \tag{S3.a}$$

where

$$\boldsymbol{\sigma} = \begin{bmatrix} \sigma_1 & 0 & 0 \\ 0 & \sigma_2 & 0 \\ 0 & 0 & \sigma_3 \end{bmatrix} = \begin{bmatrix} S_1 - P_p & 0 & 0 \\ 0 & S_2 - P_p & 0 \\ 0 & 0 & S_3 - P_p \end{bmatrix} \tag{S3.b}$$

$$\boldsymbol{R} = \begin{bmatrix} \cos a \cos b & \sin a \cos b & -\sin b \\ \cos a \sin b \sin c - \sin a \cos c & \sin a \sin b \sin c + \cos a \cos c & \cos b \sin c \\ \cos a \sin b \cos c + \sin a \sin c & \sin a \sin b \cos c - \cos b \sin c & \cos b \cos c \end{bmatrix} \tag{S3.c}$$

where S_1, S_2, and S_3 are the principal stresses, and P_p is the pore pressure at depth; the rotation angles that define the stress coordinate system in terms of geographic coordinates are as follows:

$a =$ azimuth of σ_1

$b =$ - plunge of σ_1

$c =$ rake of σ_2 ($\cong$ plunge of σ_2 in this cases)

with such transformation, the overburden stress is given by:

$$\boldsymbol{S_v} = \boldsymbol{\sigma_g}(3,3) \quad (S4)$$

Thus, for each combination of input parameters of S_v, P_p, μ, R, and stress orientations, we can calculate the principal stress (S_1, S_2, and S_3) by jointly solving Equation (S3.a), (S4), and (S5), assuming that the most favorably oriented faults are in frictional equilibrium (Brudy et al., 1997; Zoback & Healy, 1984; Zoback, 2007) with the prevailing stress field and pore pressure (P_p) at depth:

$$\frac{\sigma_1}{\sigma_3} = \frac{S_1 - P_p}{S_3 - P_p} = \left(\sqrt{\mu^2 + 1} + \mu\right)^2 \quad (S5)$$

The calculated stress state with the assumption of frictional equilibrium should be the upper bound of the in-situ stress field. Finally, we conduct the Monte Carlo simulation to evaluate the area-weighted average of fault instability *I*, i.e., I_m, using 10,000 random combinations of parameters of 304 mapped fault segments at 5 km depth where the most earthquake hypocenters are located. The resolved criticality of each fault segment by their corresponding I_m is shown in Figure 1(b), in a color-coded fashion.

Table S2. List of parameters for fault criticality analysis.

Parameter	Distribution	Mean Value	Standard Deviation	Bounds	Notes
Coefficient of friction	Truncated Gaussian	0.71	0.026	0.62 to 0.82	Distribution of 23 Measurements from Blanpied et al. (1995)
Fault strike	From map	Mapped value	2°	+/- 5°	Noise added to simulate the map uncertainty
Fault dip	Uniform	N/A	N/A	30 to 90	
Pore pressure	Uniform	N/A	N/A	46.6 to 51.5 MPa	Based on the assumed hydrostatic pore pressure gradient
Overburden stress	Truncated Gaussian	135.7	3	125.7 to 145.7 MPa	Based on the assumed rock density of 2.77 g/cm^3
Stress orientation	Truncated Gaussian	Value in Table 1	5°	+/- 10°	From stress Inversion
Shape ratio	Truncated Gaussian	Value in Table 1	0.03	+/- 0.1	From stress Inversion

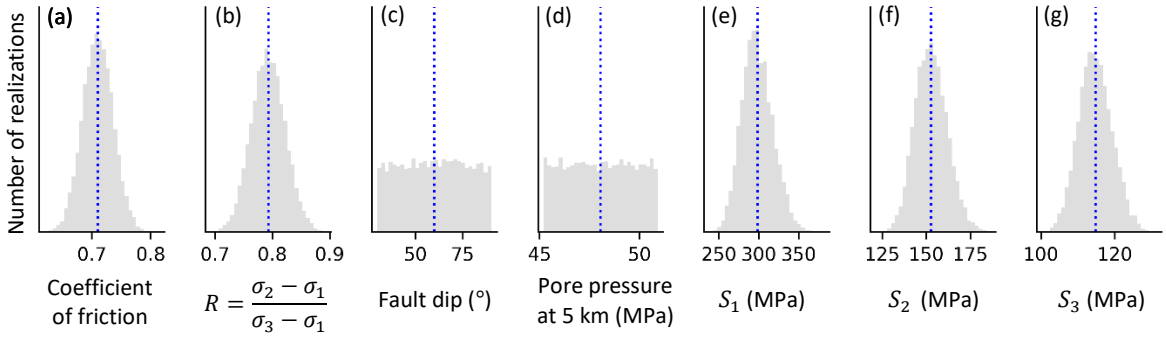

Figure S2. The uncertainties of geomechanical parameters adopted in the Monte Carlo simulation for the XLD area.

Due to the deviations of the inversed stress state from the classical assumption of in-situ stress orientation, we further evaluate the fault criticality for two extreme cases of thrust and strike-slip faulting stress environment, i.e., corresponding to the overburden stress to be minimum and second principle stress, respectively (Figure S3). It can be helpful to bound the possible range of in-situ fault instability. Here, we assume a homogeneous stress field in each area with the classical assumption of in-situ stress orientation (two is horizontal, and one is vertical). We set the azimuth of maximum principal stress to be 128° and the stress ratio R to be 0.76 (the average value of inverted results). The other parameters' distribution and the standard deviation and bounds of both stress orientation and shape ratio are the same as those shown in Table S1.

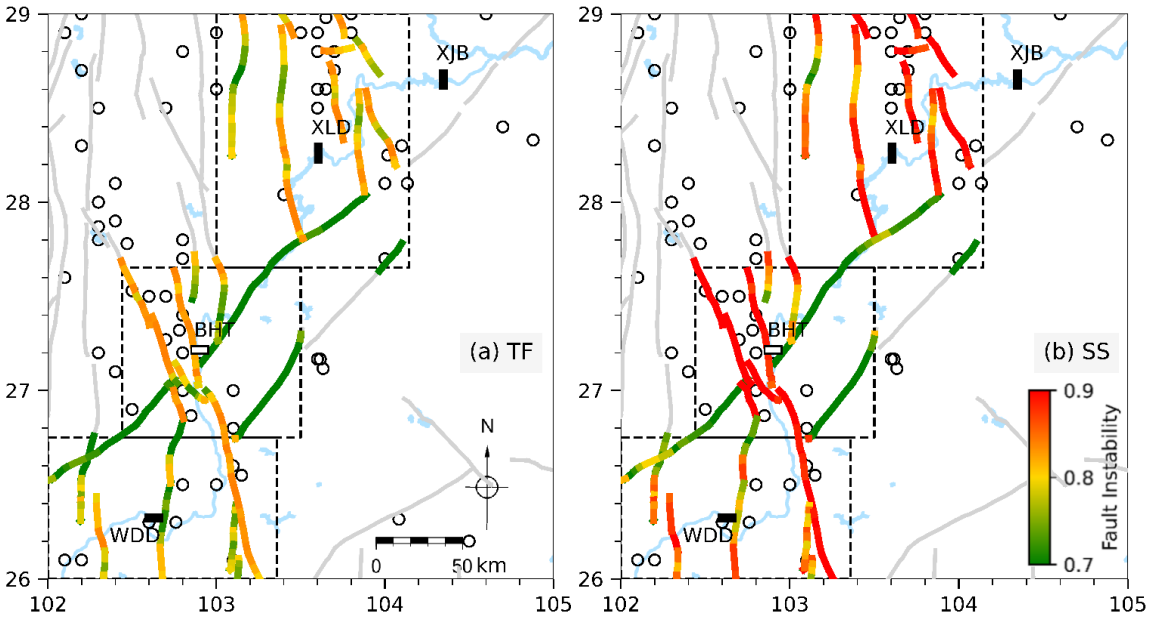

Figure S3. Same as Figure 1(b) in the main text, but with the stress environment of (a) thrust faulting (TF) and (b) strike-slip faulting (SS).

Text S2. Estimation of Hydraulic Diffusivity

The hydraulic diffusivity beneath the reservoirs has been extensively studied using reservoir-induced seismicity data (Ge et al., 2009; Guha, 2002; Roeloffs, 1988; Talwani et al., 2007). In the absence of detailed hydraulic diffusivity data in our study area, we perform the estimation through the seismicity data. The estimated local hydraulic diffusivity ranges from 0.32 to 4.6 m^2 s^{-1}, using 32 M2.5+ earthquakes within 30 km from the Xiluodu reservoir between May 6, 2013, and January 2020. This is based on the equation of $D = L^2/4t$ with L being the distances from earthquake hypocenters to the dam site and t being the lag time since May 2013 when the impoundment started.

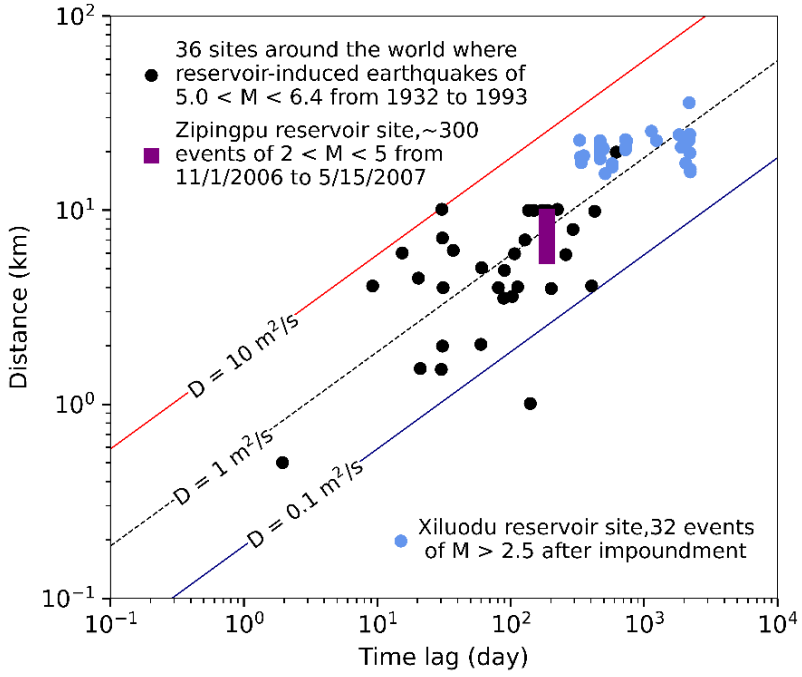

Figure S4. Inferred hydraulic diffusivity values from seismic data (modified from Ge et al. (2009)). Black dots denote the estimated hydraulic diffusivity values from Talwani et al. (2007). The purple rectangle is the estimated range of the Zipingpu reservoir from Ge et al. (2009). The blue dots are the estimated hydraulic diffusivity values from the Xiluodu reservoir using the M2.5+ earthquakes from May 2013 to January 2020.

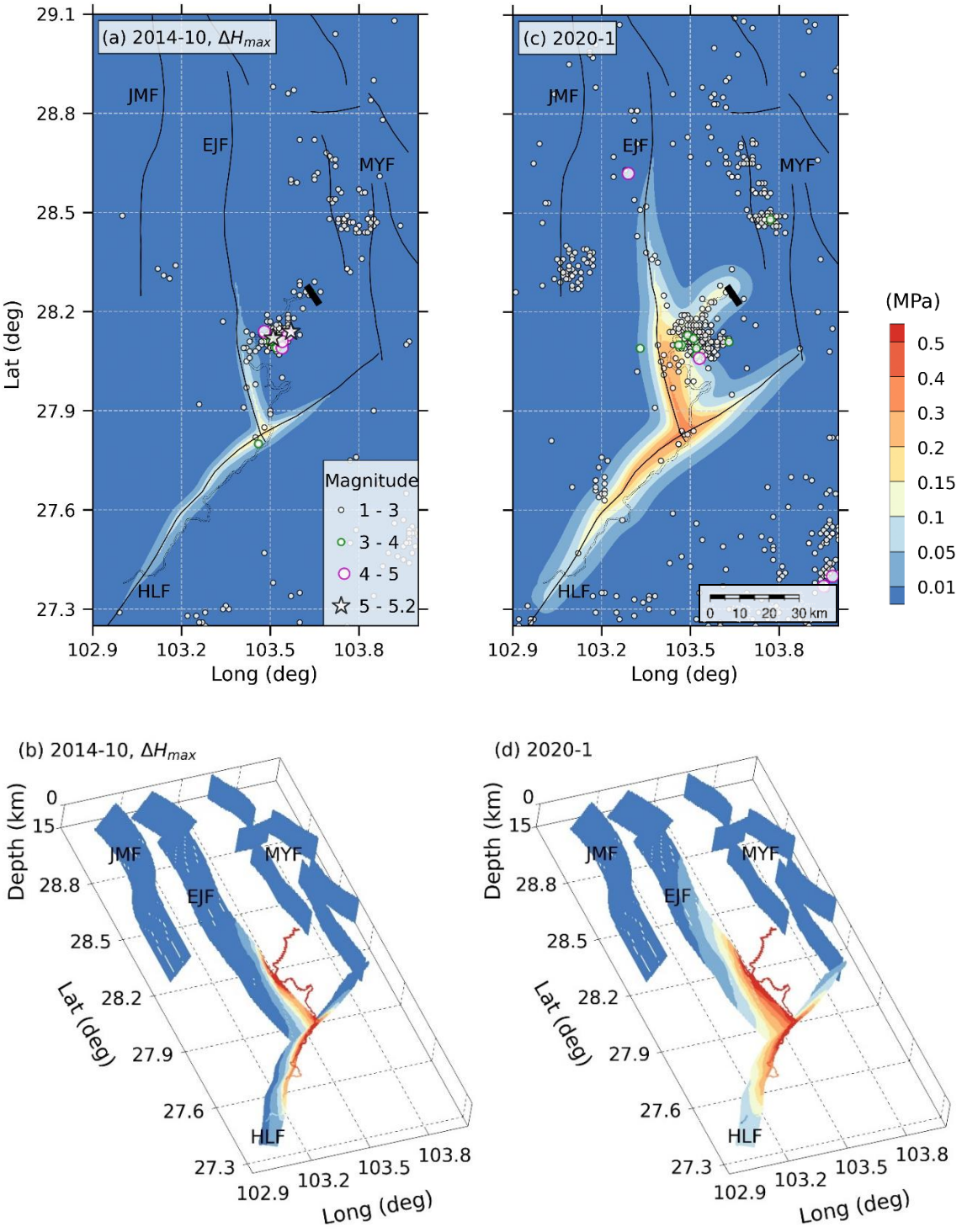

Figure S5. Same as Figure 5 in the paper, but for Case A.

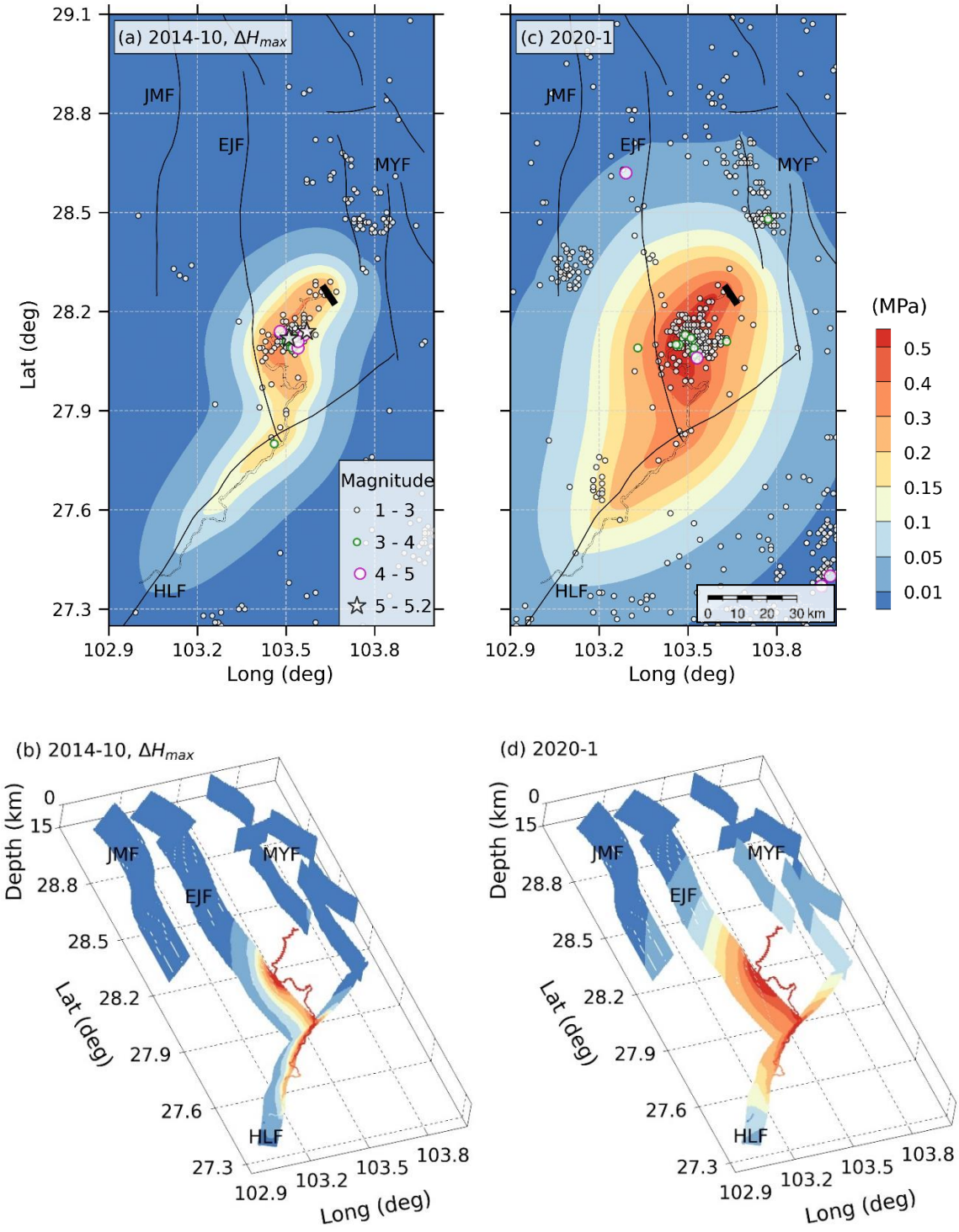

Figure S6. Same as Figure 5 in the paper, but for Case C.

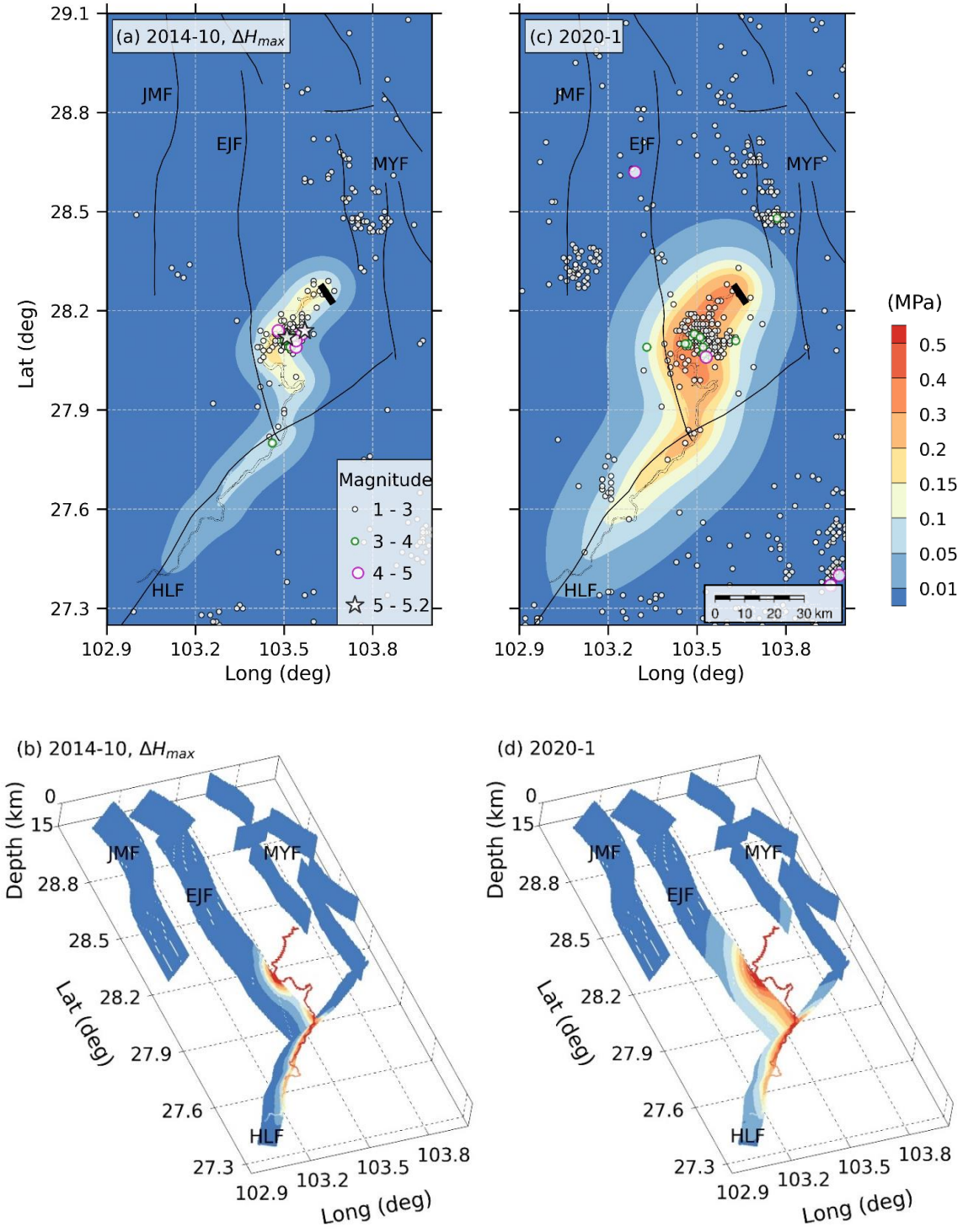

Figure S7. Same as Figure 5 in the paper, but for Case D.

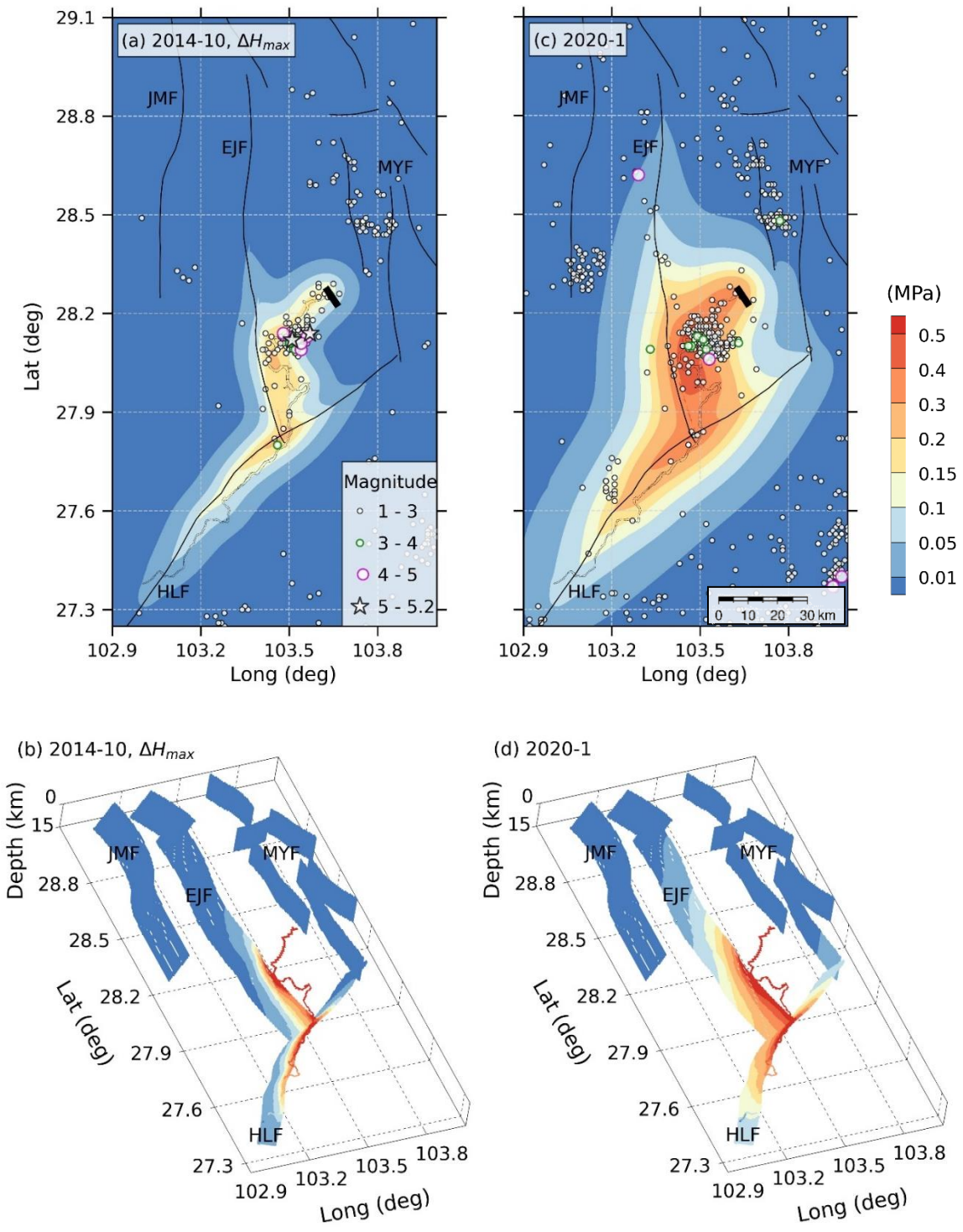

Figure S8. Same as Figure 5 in the paper, but for Case E.

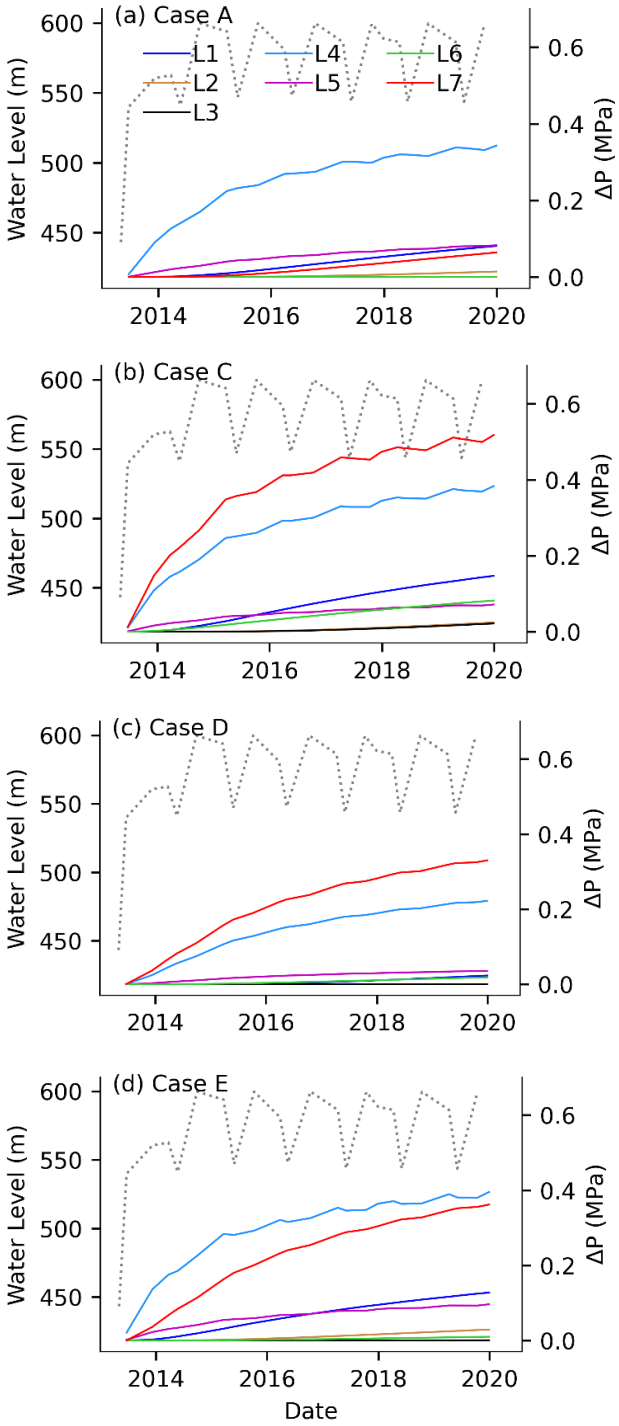

Figure S9. Same as Figure 6 in the paper, but for Case A, C, D, and E.

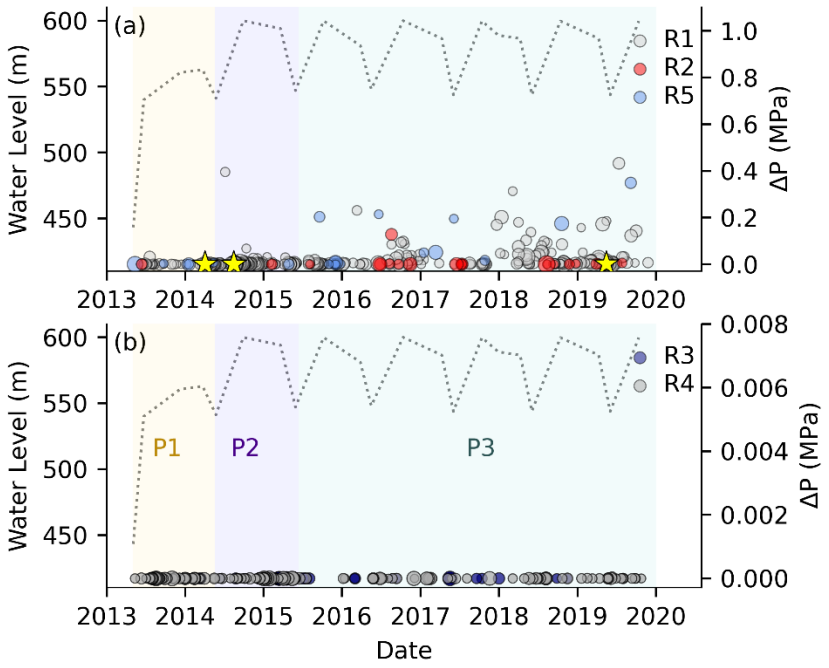

Figure S10. Same as Figure 7 in the paper, but for Case A.

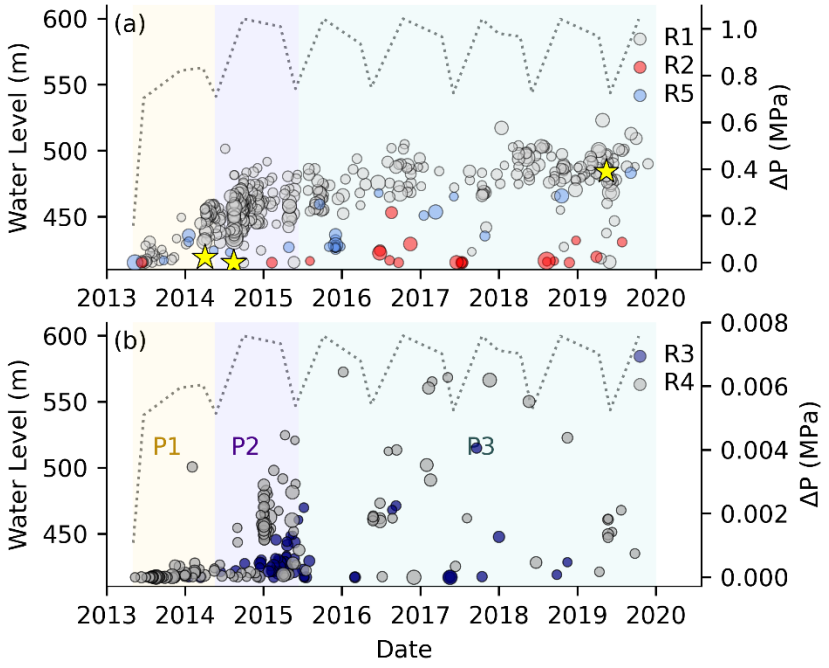

Figure S11. Same as Figure 7 in the paper, but for Case C.

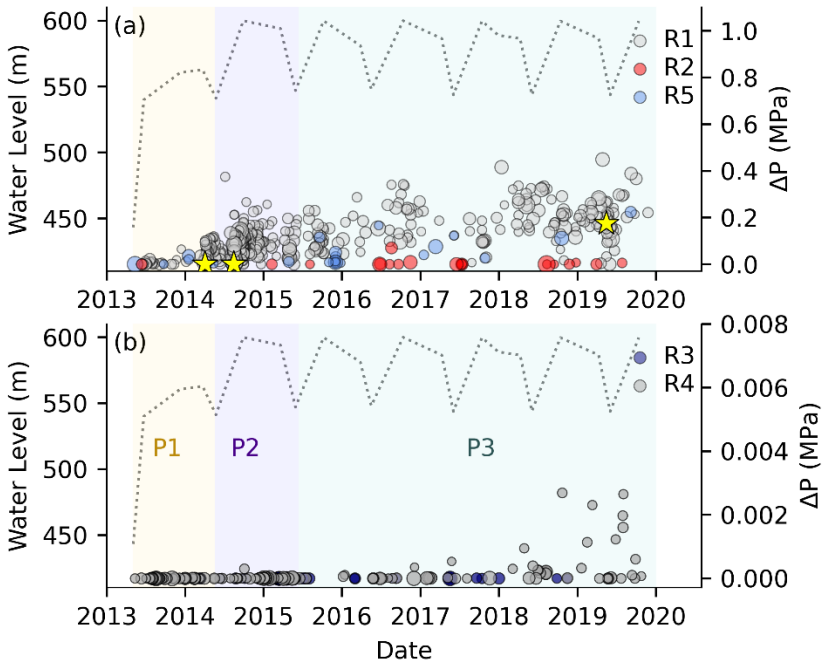

Figure S12. Same as Figure 7 in the paper, but for Case D.

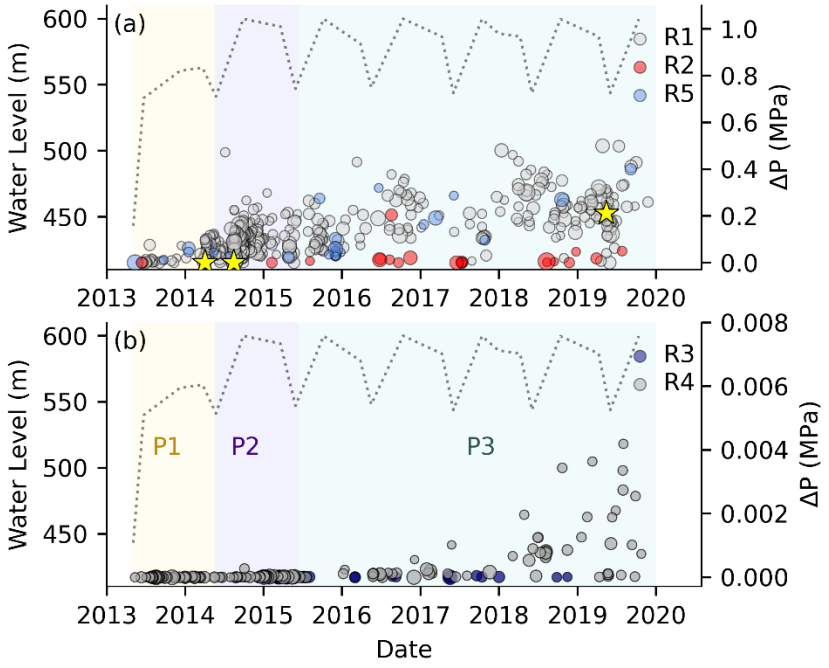

Figure S13. Same as Figure 7 in the paper, but for Case E.

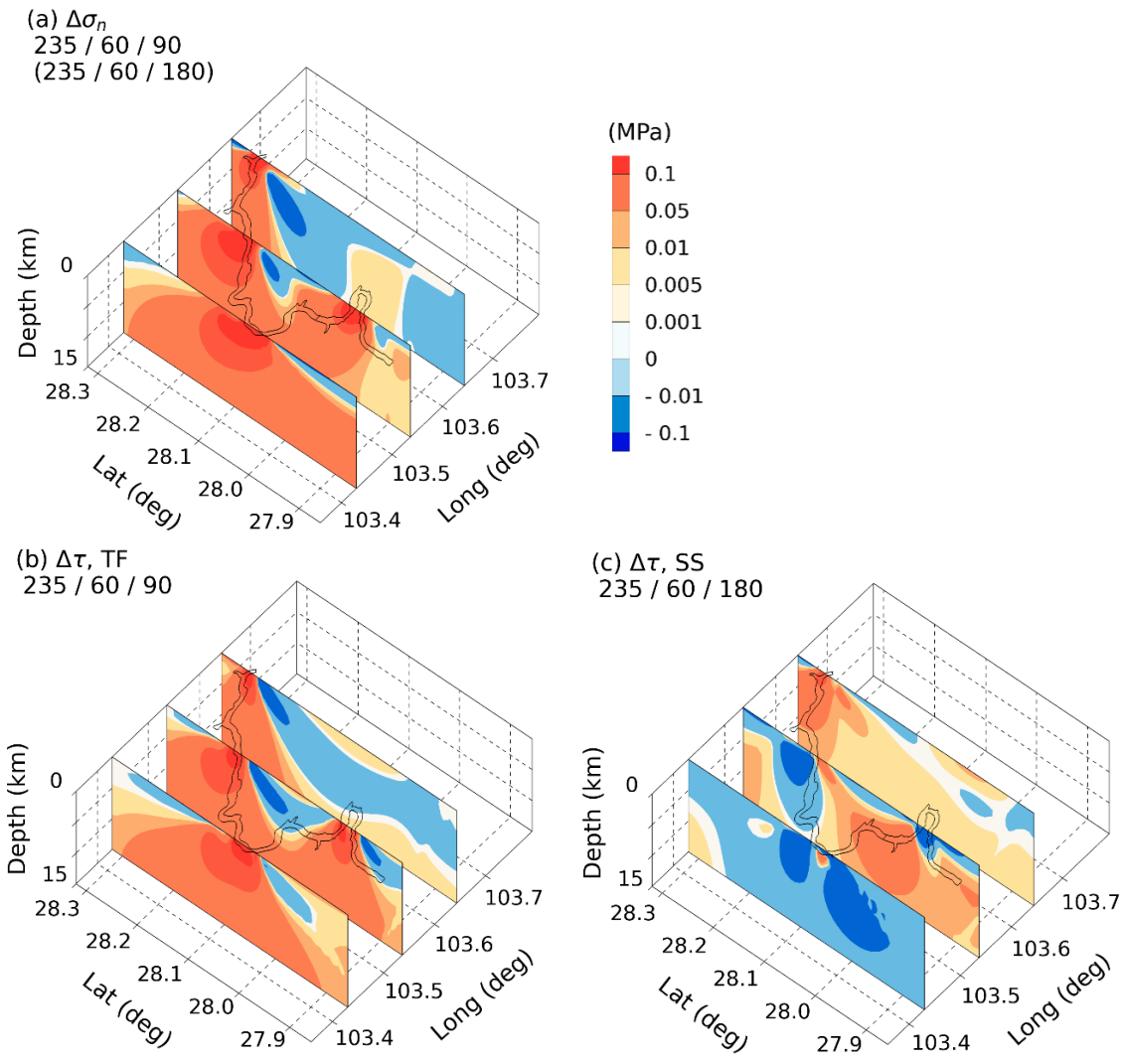

Figure S14. Spatial distribution of shear stress and normal stress in the head area of the Xiluodu reservoir, corresponding to the water level change ΔH_{max} = 160 m. The scenarios of thrust faulting (TF) and strike-slip faulting (SS) were both considered.